Double local and double nonlocal Andreev reflections in nodal-line semimetal-superconducting heterostructures

Yun-Xia Wang, Xing Wang, and Yu-Xian Li*

College of Physics and Hebei Advanced Thin Films Laboratory, Hebei Normal University, Shijiazhuang, Hebei 050024, China

(Received 10 January 2022; accepted 21 April 2022; published 2 May 2022)

Double local and double nonlocal Andreev reflections in a nodal-line semimetal-superconductor-nodal-line semimetal junction were investigated. We find that double Andreev reflections (the specular Andreev reflection and the retro-Andreev reflection), double normal reflections (the specular normal reflection and the retronormal reflection), double electron transmissions (the specular electron transmission and the normal electron transmission), and double crossed Andreev reflections (the specular crossed Andreev reflection and the crossed Andreev reflection) exist simultaneously when an electron incidents from the semimetal side. The transport properties of the scattering process depend on the incident angle, incident energy, and barrier height. It is found that a finite incident angle and a finite barrier height are necessary conditions for the appearance of these local and nonlocal Andreev reflections. By adjusting these parameters, the reflections and transmissions can be controlled.

DOI: 10.1103/PhysRevB.105.195402

I. INTRODUCTION

In recent years, a large number of new materials with massless linear excitations or nontrivial topological properties have been predicted and used to prepare structures between an ordinary conductor and a superconducting material [1–9]. In an ordinary normal metal-superconductor (NS) junction, the presence of the interface barrier provides normal electron reflection, also called specular normal reflection (SNR). For an ideal interface without barriers, only retro-Andreev reflection (RAR) takes place, where the Andreev reflection is along the original path, i.e., the hole is reflected back almost along the path of the incident electron and a Cooper pair forms in the superconductor (SC) [10]. RAR is caused by electron-hole intraband conversion, where the electron and the hole are in the same conduction or valence band. In contrast to RAR, there exists a specular Andreev reflection (SAR), which has been found in a graphene-superconductor junction, in which the hole is reflected along the specular path of the incident electron, and it is the result of electron-hole interband conversion [1,11,12]. In both structures only single Andreev reflection (SAR or RAR) occurs. In fact, the exotic phenomenon of double reflections or multiple reflections can occur in the structure based on some particular materials. For example, based on the type-II Weyl semimetal-superconductor junction, there will be double Andreev reflections (SAR and RAR) for an electron incidents from the semimetal side [13]. Particularly, in a recent study, quadruple reflections, which are the double Andreev reflections (SAR and RAR) and the double normal reflections [SNR and retronormal reflection (RNR)] [14], were found in a nodal-line semimetal-superconductor (NLSM-SC) junction.

Nodal-line semimetals (NLSMs) as a kind of three-dimensional topological material have become a hot spot in condensed matter physics [15–18]. The projection of the NLSMs on the surface of some materials will form a closed circle, which shows the tympanic topological surface states protected by topology; the Fermi level on the surface has a very high density of electronic states, so it has unique physical properties [19–29]. For example, the orbital susceptibility of NLSMs shows a stronger δ-function singularity compared to Dirac and Weyl semimetals with point nodes [30]. The quantum oscillations of NLSMs show different phase shifts from those of Weyl fermions [31]. Furthermore, NLSMs with a ring-shaped nodal line also show distinct characteristics in the transport aspects [32–36]. The unexpected nonuniversal conductance fluctuation appears in NLSMs, whose amplitude increases with the increase in spin-orbit coupling strength [37].

Most of the transport studies described above have been carried out in two-terminal systems. Actually, some three-terminal systems have a greater possibility of peculiar transport properties. In the NSN junction, four transport processes have been found to coexist simultaneously, namely, SNR, normal electron transmission (NT), RAR, and crossed Andreev reflection (CAR) [38–43]. CAR means that the incident electron enters the SC accompanied by a hole reflected from the metal on the other side. However, a study indicates that the SNR and CAR are forbidden in the type-II Weyl semimetal-SC-type-II Weyl semimetal junction, replaced by the coexistence of the double Andreev reflections (SAR and RAR) and double electron transmissions [NT and specular electron transmission (ST)] [44]. In the case of small bias, the conductance of the normal metal-superconductor junction is mainly determined by the Andreev reflection [5,45,46]. Due to the Andreev reflection results contributed by the NLSM, it is more likely that novel transport behaviors will appear based on a NLSM-SC-NLSM heterostructure. However, the

*Corresponding author: yxli@mail.hebtu.edu.cn

 ©2022 American Physical Society

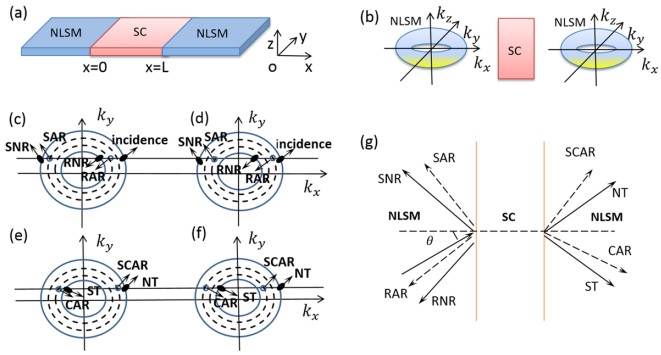

FIG. 1. (a) Schematic illustration of the NLSM-SC-NLSM junction with the nodal line perpendicular to the interface. (b) The toruslike isoenergetic surface in the NLSM. The SC plane is always parallel to the k_x-k_y plane. (c) and (e) The projection of the scattering processes on the k_x-k_y plane when $\mu_N < |E_z|$. The solid arrows denote the group velocity of ELQs (solid circles), and the dashed ones denote the group velocity of HLQs (open circles). The isoenergetic circles for ELQs (solid lines) and HLQs (dashed lines) coincide with each other for $\mu_N = 0$, but the scattering possesses similar processes. (d) and (f) The projection of the scattering processes on the k_x-k_y plane for $\mu_N > |E_z|$. The retro-Andreev and crossed Andreev reflected HLQs occupy the big isoenergetic circle, while the specular Andreev and specular crossed Andreev reflected HLQs occupy the small circle, which are different from the situation with $\mu_N < |E_z|$ in (c) and (e). (g) The projection of the eight scattering processes on the x-y plane in real space. The orange solid lines denote the NLSM-SC interface.

research on NLSMs is still lacking in the three-terminal system connected to SC, which may provide specific signatures for the research of the ring-shaped nodal line.

In this paper, we study the transport properties in the NLSM-SC-NLSM heterostructure. We find the eight scatterings coexist; that is, SAR, RAR, SNR, RNR, NT, ST, CAR, and specular crossed Andreev reflection (SCAR) can occur simultaneously. The reflection probabilities under different parameters are systematically studied. By changing the incident quasiparticle energy, incident angle, and interfacial barrier height, these eight scattering processes can be controlled.

The rest of this paper is organized as follows. In Sec. II, the Hamiltonians for NLSM and SC are given, and the expressions for wave functions and reflection probabilities for the three regions are derived. Their dependence on parameters is discussed in detail. In Sec. III, the numerical results for the amplitudes and probabilities of the eight transport processes are presented and analyzed systematically. In Sec. IV, we give a brief conclusion.

II. MODEL AND METHODS

The NLSM-SC-NLSM heterostructure we consider is shown in Fig. 1(a), which consists of two semi-infinite NLSMs and a SC of length L. The upper and lower surfaces of the SC are parallel to the x-y plane. The two interfaces are located at $x = 0$ and $x = L$, respectively, which are parallel to the y-z plane. The interfacial barrier is defined by the δ function $V(x) = V\delta(x)$. Let us think about the transport along the x direction.

We consider the two-orbit effective Hamiltonian for NLSM, which is given by [47,48]

$$\hat{H}_N(\boldsymbol{k}) = \varepsilon_k \hat{\sigma}_z - \hbar v k_z \hat{\sigma}_y - \mu_N \hat{\sigma}_0, \tag{1}$$

with $\varepsilon_k = \frac{\hbar^2}{2m}(k_x^2 + k_y^2 + k_z^2) - E_0$. $E_0 = 200\Delta$, which describes the size of the nodal line. The identity matrix $\hat{\sigma}_0$ and the Pauli matrices $\hat{\sigma}_y$ and $\hat{\sigma}_z$ are defined in orbit space. The wave vector is $\boldsymbol{k} = (k_x, k_y, k_z)$, the group velocity is $\boldsymbol{v} = (v_x, v_y, v_z)$, and μ_N is the chemical potential. For $\mu_N = 0$, the Hamiltonian describes the NLSM with a ring-shaped nodal line in the plane $k_z = 0$, while the nodal line will evolve into a torus-shaped Fermi surface for $\mu_N \neq 0$, as shown in Fig. 1(b). Here we consider the transport along the x direction with the nodal line perpendicular to the NLSM-SC interfaces at $x = 0$ and $x = L$, as shown in Fig. 1(a).

In the orbit and particle-hole coupling space, the Bogoliubov–de Gennes (BdG) Hamiltonian for the NLSM can be written as

$$\hat{H}_N(\boldsymbol{k}) = \begin{pmatrix} \hat{H}_N(\boldsymbol{k}) & 0 \\ 0 & -\hat{H}_N^*(-\boldsymbol{k}) \end{pmatrix}. \tag{2}$$

By solving the BdG equation $\hat{H}_N\psi_N = E\psi_N$ with the substitution of $-\mathbf{i}\nabla_{\mathbf{r}}$ for $\boldsymbol{k}$ in $\hat{H}_N(\boldsymbol{k})$ and $-\hat{H}_N^*(-\boldsymbol{k})$, the energy dispersions for the electronlike quasiparticles (ELQs) and the holelike quasiparticles (HLQs) can be obtained:

$$E_e^{\pm} = \pm\sqrt{\varepsilon_k^2 + E_z^2} - \mu_N \tag{3}$$

and

$$E_h^{\pm} = \pm\sqrt{\varepsilon_k^2 + E_z^2} + \mu_N, \tag{4}$$

where $E_z = \hbar v k_z$ is the orbital coupling strength. Obviously, the gap $2|E_z|$ at the nodal line is opened in the quasiparticle spectrum.

When $\mu_N = 0$, the gaps for ELQs and HLQs are symmetric with respect to zero energy, from $-|E_z|$ to $|E_z|$. The conduction band E_e^+ and valence band E_h^+ participate in the scattering processes when the incident energy E is larger than $|E_z|$, where the wave vectors k_y and k_z are conserved. The occupancy of the isoenergetic circles is the situation when the big (small) solid circle and the big (small) dashed circle coincide with each other in Fig. 1(c).

The wave function generated in the incident part of the NLSM on the left can be expressed as

$$\begin{aligned}\psi_{IN}(x<0) = &\begin{pmatrix} i\alpha \\ 1 \\ 0 \\ 0 \end{pmatrix} e^{ik_x^{e+}x} + r_{n1}\begin{pmatrix} i\alpha \\ 1 \\ 0 \\ 0 \end{pmatrix} e^{-ik_x^{e+}x} \\ &+ r_{n2}\begin{pmatrix} i\beta \\ 1 \\ 0 \\ 0 \end{pmatrix} e^{ik_x^{e-}x} + r_{a1}\begin{pmatrix} 0 \\ 0 \\ -i\beta \\ 1 \end{pmatrix} e^{-ik_x^{h+}x} \\ &+ r_{a2}\begin{pmatrix} 0 \\ 0 \\ -i\alpha \\ 1 \end{pmatrix} e^{ik_x^{h-}x},\end{aligned} \tag{5}$$

with $\alpha = (E + \sqrt{E^2 - E_z^2})/E_z$, $\beta = (E - \sqrt{E^2 - E_z^2})/E_z$ and $k_x^{e(h)\pm} = \sqrt{\frac{2m}{\hbar^2}(E_0 \pm \sqrt{E^2 - \hbar^2 v^2 k_z^2}) - k_y^2 - k_z^2}$. The coefficients r_{n1}, r_{n2}, r_{a1}, and r_{a2} represent reflection amplitudes for SNR, RNR, SAR, and RAR, respectively.

When $\mu_N \neq 0$, the two gaps are not symmetrical about $E = 0$, and the discussion is divided into two cases. The first case is $\mu_N < |E_z|$, and the scattering processes are shown in Fig. 1(c). The wave function generated in the incident part of the left NLSM at $\mu_N < |E_z|$ is expressed as

$$\begin{aligned}\psi_{IN}(x<0) = &\begin{pmatrix} i\lambda_{11} \\ 1 \\ 0 \\ 0 \end{pmatrix} e^{ik_x^{e+}x} + r_{n1}\begin{pmatrix} i\lambda_{11} \\ 1 \\ 0 \\ 0 \end{pmatrix} e^{-ik_x^{e+}x} \\ &+ r_{n2}\begin{pmatrix} i\lambda_{12} \\ 1 \\ 0 \\ 0 \end{pmatrix} e^{ik_x^{e-}x} + r_{a1}\begin{pmatrix} 0 \\ 0 \\ -i\lambda_{22} \\ 1 \end{pmatrix} e^{-ik_x^{h+}x} \\ &+ r_{a2}\begin{pmatrix} 0 \\ 0 \\ -i\lambda_{21} \\ 1 \end{pmatrix} e^{ik_x^{h-}x}, \end{aligned} \tag{6}$$

with $\lambda_{11(12)} = [E + \mu_N + (-)N^+]/E_z$, $\lambda_{21(22)} = [E - \mu_N + (-)N^-]/E_z$, $k_x^{e\pm} = \sqrt{\frac{2m}{\hbar^2}(E_0 \pm N^+) - k_y^2 - k_z^2}$, $k_x^{h\pm} = \sqrt{\frac{2m}{\hbar^2}(E_0 \pm N^-) - k_y^2 - k_z^2}$, and $N^\pm = \sqrt{(E \pm \mu_N)^2 - E_z^2}$. The coefficients r_{n1}, r_{n2}, r_{a1}, and r_{a2} are the same as those in Eq. (5). As $\mu_N \to 0$, the wave function in Eq. (6) degenerates into that in Eq. (5).

The second case is $\mu_N > |E_z|$. Since the gap in HLQs ranges from $-|E_z| + \mu_N > 0$ to $|E_z| + \mu_N > 0$, there are two more situations. The one is $0 < E < -|E_z| + \mu_N$. The conduction bands E_e^+ and E_h^- participate in the scattering processes at this time, and they are shown in Fig. 1(d). The wave function in the incident part of the NLSM is

$$\begin{aligned}\psi_{IN}(x<0) = &\begin{pmatrix} i\lambda_{11} \\ 1 \\ 0 \\ 0 \end{pmatrix} e^{ik_x^{e+}x} + r_{n1}\begin{pmatrix} i\lambda_{11} \\ 1 \\ 0 \\ 0 \end{pmatrix} e^{-ik_x^{e+}x} \\ &+ r_{n2}\begin{pmatrix} i\lambda_{12} \\ 1 \\ 0 \\ 0 \end{pmatrix} e^{ik_x^{e-}x} + r_{a1}\begin{pmatrix} 0 \\ 0 \\ -i\lambda_{21} \\ 1 \end{pmatrix} e^{-ik_x^{h-}x} \\ &+ r_{a2}\begin{pmatrix} 0 \\ 0 \\ -i\lambda_{22} \\ 1 \end{pmatrix} e^{ik_x^{h+}x}, \end{aligned} \tag{7}$$

where λ_{11}, λ_{12}, λ_{21}, λ_{22}, $k_x^{e\pm}$, and $k_x^{h\pm}$ have the same meanings as in Eq. (6). The other situation is $E > |E_z| + \mu_N$; then the energy bands participating in the scattering processes become the conduction band E_e^+ and valence band E_h^+. The wave function reverts to Eq. (6).

In this paper, we consider the s-wave pairing superconductivity. The Hamiltonian for the SC part is

$$\hat{H}_S(\boldsymbol{k}) = \begin{pmatrix} \hat{H}_S(\boldsymbol{k}) & \hat{\Delta} \\ \hat{\Delta} & -\hat{H}_S^*(-\boldsymbol{k}) \end{pmatrix}, \tag{8}$$

in which $\hat{H}_S(\boldsymbol{k}) = \varepsilon_k \hat{\sigma}_z - \hbar v k_z \hat{\sigma}_y - \mu_S \hat{\sigma}_0$ and $\hat{\Delta} = \Delta \hat{\sigma}_0$. Δ is the superconducting gap magnitude, and μ_S is the chemical potential in the SC.

The wave function of the SC is

$$\begin{aligned}\psi_{IIS}(0<x<L) = &A_1\begin{pmatrix} iu\eta_{11} \\ u \\ i\eta_{11} \\ 1 \end{pmatrix} e^{ip_x^+x} + A_2\begin{pmatrix} iu\eta_{11} \\ u \\ i\eta_{11} \\ 1 \end{pmatrix} e^{-ip_x^+x} \\ &+ A_3\begin{pmatrix} iu\eta_{12} \\ u \\ i\eta_{12} \\ 1 \end{pmatrix} e^{ip_x^-x} + A_4\begin{pmatrix} iu\eta_{12} \\ u \\ i\eta_{12} \\ 1 \end{pmatrix} e^{-ip_x^-x} \\ &+ A_5\begin{pmatrix} iv\eta_{21} \\ v \\ i\eta_{21} \\ 1 \end{pmatrix} e^{iq_x^+x} + A_6\begin{pmatrix} iv\eta_{21} \\ v \\ i\eta_{21} \\ 1 \end{pmatrix} e^{-iq_x^+x} \\ &+ A_7\begin{pmatrix} iv\eta_{22} \\ v \\ i\eta_{22} \\ 1 \end{pmatrix} e^{iq_x^-x} + A_8\begin{pmatrix} iv\eta_{22} \\ v \\ i\eta_{22} \\ 1 \end{pmatrix} e^{-iq_x^-x}, \end{aligned} \tag{9}$$

where $u = (E + S)/\Delta$, $v = (E - S)/\Delta$, $\eta_{11(12)} = [\mu_S + S + (-)S^+]/E_z$, and $\eta_{21(22)} = [\mu_S - S + (-)S^-]/E_z$, with $S = \sqrt{E^2 - \Delta^2}$ and $S^\pm = \sqrt{(S \pm \mu_S)^2 - E_z^2}$. The wave vectors $p_x^\pm = \sqrt{\frac{2m}{\hbar^2}(E_0 \pm S^+) - k_y^2 - k_z^2}$, and $q_x^\pm = \sqrt{\frac{2m}{\hbar^2}(E_0 \pm S^-) - k_y^2 - k_z^2}$. The symbols A_1, A_2, A_3, A_4, A_5, A_6, A_7, and A_8 are coefficients of the quasiparticle modes in the SC region.

Similarly, the wave function generated in the NLSM on the right side of the SC, when $\mu_N = 0$, is expressed as

$$\begin{aligned}\psi_{IIIN}(x>L) = &t_1\begin{pmatrix} i\alpha \\ 1 \\ 0 \\ 0 \end{pmatrix} e^{ik_x^{e+}x} + t_2\begin{pmatrix} i\beta \\ 1 \\ 0 \\ 0 \end{pmatrix} e^{-ik_x^{e-}x} \\ &+ t_3\begin{pmatrix} 0 \\ 0 \\ -i\beta \\ 1 \end{pmatrix} e^{ik_x^{h+}x} + t_4\begin{pmatrix} 0 \\ 0 \\ -i\alpha \\ 1 \end{pmatrix} e^{-ik_x^{h-}x}. \end{aligned} \tag{10}$$

The wave function for $\mu_N < |E_z|$ or $\mu_N > |E_z|$ and $E > |E_z| + \mu_N$ can be defined as

$$\begin{aligned}\psi_{IIIN}(x>L) = &t_1\begin{pmatrix} i\lambda_{11} \\ 1 \\ 0 \\ 0 \end{pmatrix} e^{ik_x^{e+}x} + t_2\begin{pmatrix} i\lambda_{12} \\ 1 \\ 0 \\ 0 \end{pmatrix} e^{-ik_x^{e-}x} \\ &+ t_3\begin{pmatrix} 0 \\ 0 \\ -i\lambda_{22} \\ 1 \end{pmatrix} e^{ik_x^{h+}x} + t_4\begin{pmatrix} 0 \\ 0 \\ -i\lambda_{21} \\ 1 \end{pmatrix} e^{-ik_x^{h-}x}, \end{aligned} \tag{11}$$

and for $\mu_N > |E_z|$ and $0 < E < -|E_z| + \mu_N$, it can be written as

$$\psi_{IIIN}(x > L) = t_1 \begin{pmatrix} i\lambda_{11} \\ 1 \\ 0 \\ 0 \end{pmatrix} e^{ik_x^{e+}x} + t_2 \begin{pmatrix} i\lambda_{12} \\ 1 \\ 0 \\ 0 \end{pmatrix} e^{-ik_x^{e-}x} + t_3 \begin{pmatrix} 0 \\ 0 \\ -i\lambda_{21} \\ 1 \end{pmatrix} e^{ik_x^{h-}x} + t_4 \begin{pmatrix} 0 \\ 0 \\ -i\lambda_{22} \\ 1 \end{pmatrix} e^{-ik_x^{h+}x}, \tag{12}$$

where α and β are the same as those in Eq. (5) and λ_{11}, λ_{12}, λ_{21}, and λ_{22} are the same as those in Eq. (6). The coefficients t_1, t_2, t_3, and t_4 are the amplitudes of NT, ST, SCAR, and CAR, respectively. For $\mu_N = 0$, the isoenergetic circles of ELQs (solid lines) and HLQs (dashed lines) coincide, and the scattering processes are the same as in the case when the isoenergetic circles of Fig. 1(e) coincide. The scattering is shown in Fig. 1(e) for $\mu_N < |E_z|$ or $\mu_N > |E_z|$ and $E > |E_z| + \mu_N$. As for $\mu_N > |E_z|$ and $0 < E < -|E_z| + \mu_N$, the scattering is shown in Fig. 1(f).

There are two types of incident ELQs from the NLSM; one is an incident wave with a wave vector $\boldsymbol{k} = (k_x^{e+}, k_y, k_z)$, and the other is an incident wave with $\boldsymbol{k} = (-k_x^{e-}, k_y, k_z)$. Moreover, no matter which incident wave (k_x^{e+} or $-k_x^{e-}$) is used, there are always eight scattering processes: the double Andreev reflections (SAR and RAR) with the wave vectors $\boldsymbol{k} = (-k_x^{h+}, k_y, k_z)$ and (k_x^{h-}, k_y, k_z), the double normal reflections (SNR and RNR) with $\boldsymbol{k} = (-k_x^{e+}, k_y, k_z)$ and (k_x^{e-}, k_y, k_z), the double crossed Andreev reflections (SCAR and CAR) with $\boldsymbol{k} = (k_x^{h+}, k_y, k_z)$ and $(-k_x^{h-}, k_y, k_z)$, and the double electron transmissions (NT and ST) with $\boldsymbol{k} = (k_x^{e+}, k_y, k_z)$ and $(-k_x^{e-}, k_y, k_z)$, as shown in Figs. 1(c)–1(f).

The reflection and transmission amplitudes can be obtained with the following boundary conditions:

$$\begin{aligned} &\psi_{IN}(x = 0^-) = \psi_{IIS}(x = 0^+), \\ &\psi'_{IIS}(x = 0^+) - \psi'_{IN}(x = 0^-) = \frac{2mV}{\hbar^2}\hat{M}\psi_{IN}(x = 0), \\ &\psi_{IIS}(x = L^-) = \psi_{IIIN}(x = L^+), \\ &\psi'_{IIIN}(x = L^+) - \psi'_{IIS}(x = L^-) = \frac{2mV}{\hbar^2}\hat{M}\psi_{IIIN}(x = L), \end{aligned} \tag{13}$$

where $\hat{M}$ is a 4×4 diagonal matrix with diagonal elements $(1, -1, 1, -1)$. We define the wave vector $k_0 = \sqrt{2m\Delta/\hbar^2}$, and the effective barrier height is given by $V_0 = \frac{2mV}{\hbar^2 k_0}$.

The probabilities of SNR, RNR, NT, and ST are

$$\begin{aligned} S_{NR} &= |r_{n1}|^2, \\ R_{NR} &= \mathrm{Re}\left[\frac{k_x^{e-}}{k_x^{e+}}\right]|r_{n2}|^2\left|\frac{\lambda_{12}^2 - 1}{\lambda_{11}^2 - 1}\right|, \\ T_{eR} &= |t_1|^2, \end{aligned} \tag{14}$$

$$T_{eS} = \mathrm{Re}\left[\frac{k_x^{e-}}{k_x^{e+}}\right]|t_2|^2\left|\frac{\lambda_{12}^2 - 1}{\lambda_{11}^2 - 1}\right|. \tag{15}$$

For $\mu_N < |E_z|$ or $\mu_N > |E_z|$ and $E > |E_z| + \mu_N$, the probabilities of SAR, RAR, SCAR, and CAR are

$$\begin{aligned} S_{AR} &= \mathrm{Re}\left[\frac{k_x^{h+}}{k_x^{e+}}\right]|r_{a1}|^2\left|\frac{\lambda_{22}^2 - 1}{\lambda_{11}^2 - 1}\right|, \\ R_{AR} &= \mathrm{Re}\left[\frac{k_x^{h-}}{k_x^{e+}}\right]|r_{a2}|^2\left|\frac{\lambda_{21}^2 - 1}{\lambda_{11}^2 - 1}\right|, \\ T_{hR} &= \mathrm{Re}\left[\frac{k_x^{h+}}{k_x^{e+}}\right]|t_3|^2\left|\frac{\lambda_{22}^2 - 1}{\lambda_{11}^2 - 1}\right|, \end{aligned} \tag{16}$$

$$T_{hS} = \mathrm{Re}\left[\frac{k_x^{h-}}{k_x^{e+}}\right]|t_4|^2\left|\frac{\lambda_{21}^2 - 1}{\lambda_{11}^2 - 1}\right|. \tag{17}$$

For $\mu_N > |E_z|$ and $0 < E < -|E_z| + \mu_N$, the probabilities of SAR, RAR, SCAR, and CAR are

$$\begin{aligned} S_{AR} &= \mathrm{Re}\left[\frac{k_x^{h-}}{k_x^{e+}}\right]|r_{a1}|^2\left|\frac{\lambda_{21}^2 - 1}{\lambda_{11}^2 - 1}\right|, \\ R_{AR} &= \mathrm{Re}\left[\frac{k_x^{h+}}{k_x^{e+}}\right]|r_{a2}|^2\left|\frac{\lambda_{22}^2 - 1}{\lambda_{11}^2 - 1}\right|, \\ T_{hR} &= \mathrm{Re}\left[\frac{k_x^{h-}}{k_x^{e+}}\right]|t_3|^2\left|\frac{\lambda_{21}^2 - 1}{\lambda_{11}^2 - 1}\right|, \end{aligned} \tag{18}$$

$$T_{hS} = \mathrm{Re}\left[\frac{k_x^{h+}}{k_x^{e+}}\right]|t_4|^2\left|\frac{\lambda_{22}^2 - 1}{\lambda_{11}^2 - 1}\right|. \tag{19}$$

The reflection amplitudes $\tilde{r}_{n1}$, $\tilde{r}_{n2}$, $\tilde{r}_{a1}$, $\tilde{r}_{a2}$, $\tilde{t}_3$, and $\tilde{t}_4$ and the corresponding probabilities $\tilde{S}_{NR}$, $\tilde{R}_{NR}$, $\tilde{S}_{AR}$, $\tilde{R}_{AR}$, $\tilde{T}_{hR}$, and $\tilde{T}_{hS}$, as well as the transmission amplitudes $\tilde{t}_1$ and $\tilde{t}_2$ and the corresponding probabilities $\tilde{T}_{eR}$ and $\tilde{T}_{eS}$ of an incident ELQ with wave vector $-k_x^{e-}$, can be calculated in the same way. The probabilities satisfy the conservation conditions,

$$\begin{aligned} &S_{NR} + R_{NR} + S_{AR} + R_{AR} + T_{eR} + T_{eS} + T_{hR} + T_{hS} = 1, \\ &\tilde{S}_{NR} + \tilde{R}_{NR} + \tilde{S}_{AR} + \tilde{R}_{AR} + \tilde{T}_{eR} + \tilde{T}_{eS} + \tilde{T}_{hR} + \tilde{T}_{hS} = 1. \end{aligned} \tag{20}$$

III. RESULTS AND DISCUSSION

Here only the numerical results and analysis of the incident ELQs with wave vector k_x^{e+} are given in detail. We take $\mu_N = \mu_S$ to eliminate the wave vector mismatch caused by the difference in chemical potential between the NLSM and SC. In this paper, the unit of length is $\xi = hv/\Delta$, and the energy unit is Δ.

The reflection probabilities for electrons and holes as a function of incident angle θ with different incident energies E are shown in Fig. 2. From Fig. 2, we can see that the coefficients are always symmetric about $\theta = 0$. In this case, the band gap of ELQs ranges from -0.8Δ to -0.2Δ, while that of HLQs ranges from 0.2Δ to 0.8Δ. When $0 < E < 0.2\Delta$, only the ELQs located on the conduction band E_e^+ and the HLQs located on the conduction band E_h^- can participate in the scattering processes, as shown in Fig. 1(d). Double Andreev reflections and double normal reflections exist simultaneously. When $E = 0.1\Delta$, ELQs and HLQs meet this

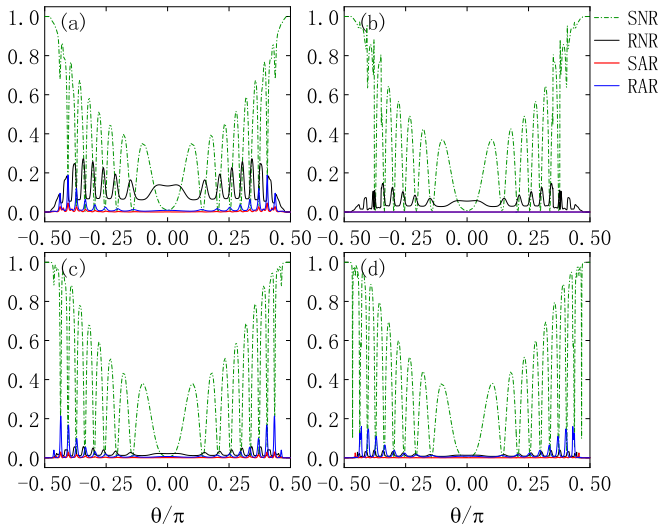

FIG. 2. The reflection probabilities for electrons and holes as functions of the incident angle θ with different incident energies E. $\mu_N = \mu_S = 0.5\Delta$, $E_z = 0.3\Delta$, $V_0 = 10$, and $L = 1.5\xi$. (a) $E = 0.1\Delta$, (b) $E = 0.4\Delta$, (c) $E = 0.9\Delta$, and (d) $E = 1.3\Delta$.

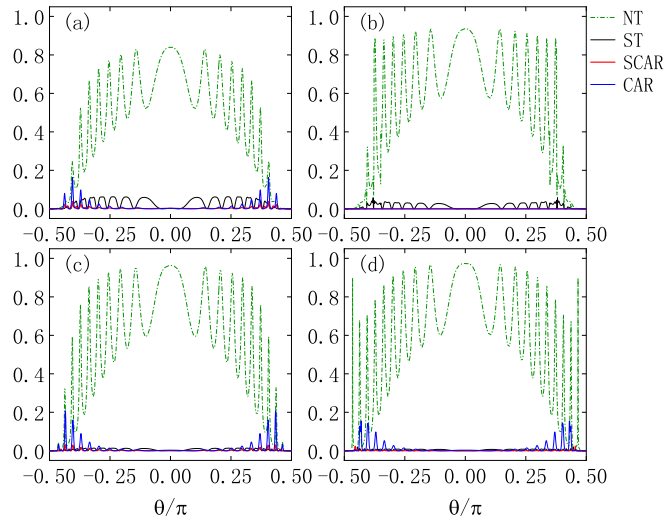

FIG. 3. The transmission probabilities as a function of incident angles for $\mu_N = \mu_S = 0.5\Delta$, $E_z = 0.3\Delta$, $V_0 = 10$, and $L = 1.5\xi$. (a) $E = 0.1\Delta$, (b) $E = 0.4\Delta$, (c) $E = 0.9\Delta$, and (d) $E = 1.3\Delta$.

requirement; the four reflection probabilities are all nonzero, as shown in Fig. 2(a). As θ increases from zero to $\pi/2$, the probability of SNR gradually increases, while for RNR, SAR, and RAR, both increase first and then decrease. The double Andreev reflections are almost zero near $\theta = 0$, then exhibit oscillations and reach a maximal peak at $\theta = 0.4\pi$. Therefore, a finite incident angle is necessary for the Andreev reflections.

When $0.2\Delta < E < 0.8\Delta$, only ELQs located on the conduction band E_e^+ can participate in the scattering processes. The incident energy is within the band gap of HLQs when $E = 0.4\Delta$, resulting in the disappearance of the double Andreev reflections and SAR = RAR = 0, as shown in Fig. 2(b). When $E > 0.8\Delta$, the HLQs located on the valence band E_h^+ are activated and participate in the scattering processes, as shown in Fig. 1(c). The four reflections appear simultaneously, as shown in Figs. 2(c) and 2(d). This case is different from those in Fig. 2(a), where the maximal peak positions of the double Andreev reflections move to a larger angle; that is, the maximal peak positions become $\theta = 0.45\pi$. It can be seen that in this energy range, a larger incident angle is favorable to the Andreev reflections. However, when we continue to increase the incident energy E; it is found that the double Andreev reflection probabilities are weakened by comparing Fig. 2(c) with Fig. 2(d). This is because when $E > \Delta$, the tunneling of quasiparticles is enhanced; as a result, the reflection probabilities will decrease.

The transmission probabilities for electrons and holes as a function of incident angle θ with different incident energies E are shown in Fig. 3. The band gaps of ELQs and HLQs are the same as those in Fig. 2. When $0 < E < 0.2\Delta$, the ELQs on the conduction band E_e^+ and the HLQs on the conduction band E_h^- participate in the scattering processes, and the scattering processes in the NLSM on the right end are shown in Fig. 1(f). The double crossed Andreev reflections and double electron transmissions exist simultaneously. As shown in Fig. 3(a), the four probabilities are all nonzero for $E = 0.1\Delta$. As θ increases from zero to $\pi/2$, the probability of NT decreases, the probabilities of ST, SCAR, and CAR show oscillations and increase first and then decrease. The probabilities of SCAR and CAR are almost zero near $\theta = 0$. Therefore, a finite incident angle is a necessary condition for the crossed Andreev reflections to occur.

When $E = 0.4\Delta$, the incident energy is located in the gap of HLQs; as a result, the crossed Andreev reflections disappear, as shown in Fig. 3(b). When $E > 0.8\Delta$, the ELQs on the conduction band E_e^+ and the reactivated HLQs on the valence band E_h^+ participate in the scattering processes, as shown in Fig. 1(e). At this point, four transmissions reappear simultaneously, as shown in Figs. 3(c) and 3(d). It is obvious that the variation is similar to the reflection probabilities; that is, the larger E is, the smaller the probabilities of the double crossed Andreev reflections are.

Now, we focus on the Andreev reflections and crossed Andreev reflections. Figure 4 shows the probabilities of SAR, RAR, SCAR, and CAR as a function of θ with different interfacial barriers. According to the above parameters, the conduction band E_e^+ and the valence band E_h^+ in the scattering processes can be obtained. In principle, the four probabilities should be nonzero. Nevertheless, when $V_0 = 0$, none of the four probabilities appear, as shown in Figs. 4(a)–4(d). For a finite barrier height V_0, even at very small $V_0 = 2$, the double Andreev reflections and the double crossed Andreev reflections immediately appear. Consequently, a finite barrier height is one of the necessary conditions for the occurrence of the double Andreev reflections and double crossed Andreev reflections.

The four Andreev reflections have the same properties: the reflection coefficients reach their maximal peaks near the larger incident angle $\theta = 0.45\pi$ with a smaller $V_0 = 2$. However, when we continue to increase V_0, their maximal peaks are around $\theta = 0.4\pi$. So for a smaller V_0, a larger incident angle is more conducive to the double crossed Andreev reflections and double Andreev reflections.

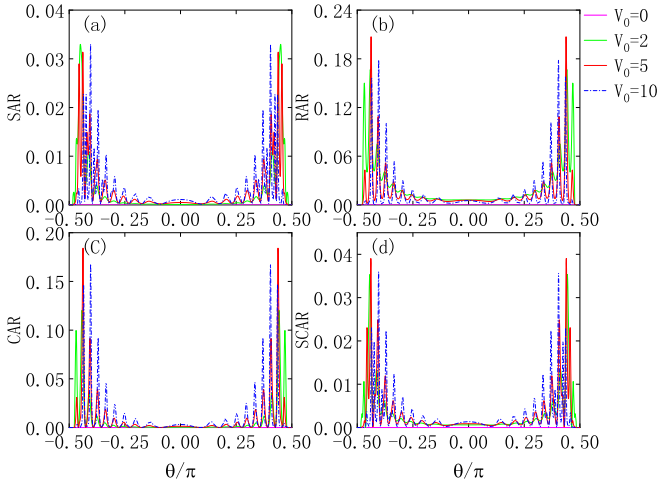

FIG. 4. The double Andreev reflection probabilities and double crossed Andreev reflection probabilities as a function of incident angle for $E = 0.7\Delta$, $\mu_N = \mu_S = 0.2\Delta$, $E_z = 0.4\Delta$, and $L = 1.5\xi$ with different V_0.

Figure 5 shows the variation of the reflection and transmission probabilities vs incident energy for different incident angles. Because the Andreev reflections are not obvious for small incident angles, only the larger incident angles ($\theta \geqslant 0.4\pi$) are shown in Fig. 5. When the incident angle θ is too small, only NT and SNR can occur; the other six scattering processes are suppressed almost completely. This is because the incident angle is too small to meet the conditions for the Andreev reflections to occur. Thus, a finite incident angle is one of the necessary conditions for the occurrence of Andreev reflections, which is consistent with the previous conclusions in Figs. 2 and 3.

From the parameters shown in Fig. 5, it can be calculated that the band gap of ELQs ranges from -0.9Δ to -0.5Δ, while that of HLQs ranges from 0.5Δ to 0.9Δ. Therefore,

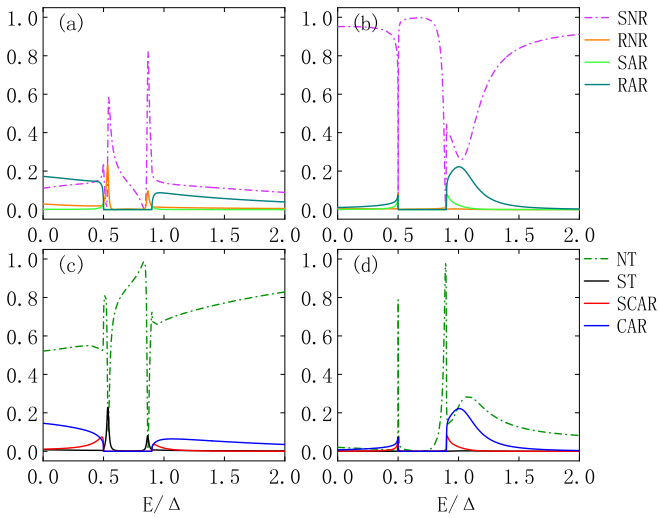

FIG. 5. (a) and (b) The reflection probabilities and (c) and (d) the transmission probabilities as a function of incident energy with different incident angles. $\mu_N = \mu_S = 0.7\Delta$, $E_z = 0.2\Delta$, $V_0 = 10$, and $L = \xi$. (a) and (c) $\theta = 0.4\pi$ and (b) and (d) $\theta = 0.45\pi$.

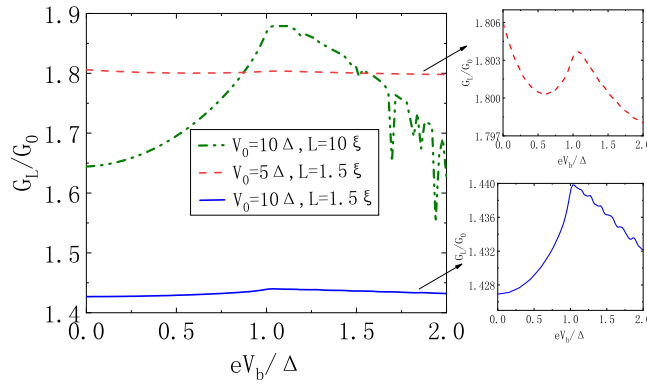

FIG. 6. The local conductance as a function of eV_b with different V_0 and L for $\mu_N = \mu_S = 5\Delta$.

when the incident energy is within the band gap range of HLQs, $0.5\Delta < E < 0.9\Delta$, neither Andreev reflections (SAR and RAR) nor crossed Andreev reflections (SCAR and CAR) can appear, as shown in Figs. 5(a)–5(d). Once the incident energy exceeds this range, $E < 0.5\Delta$ or $E > 0.9\Delta$, both the Andreev reflections and the crossed Andreev reflections appear immediately. The Andreev reflections occur from the conduction band E_h^- involved in scattering for $E < 0.5\Delta$, while the Andreev reflections occur from the valence band E_h^+ involved in scattering for $E > 0.9\Delta$. When the incident energy $E > \Delta$, the reflection probabilities of SAR, RAR, SCAR, and CAR decrease due to the enhancement of quasiparticle tunneling, and the probability of NT will increase as expected, as shown in Figs. 5(a) and 5(c). Especially, if the incident angle is too large, the probability of NT will decrease at $E > \Delta$, while that for SNR will increase, as shown in Figs. 5(b) and 5(d). Therefore, a large incident angle ($\theta \geqslant 0.45\pi$) will facilitate SNR and weaken NT at $E > \Delta$.

Next, let us investigate the differential conductance. According to the Blonder-Tinkham-Klapwijk (BTK) formula [49], the local conductance G_L can be written as

$$G_L = \frac{2e^2}{h}\frac{S}{(2\pi)^2}\frac{\sqrt{2mE_0}}{\hbar^2 v}\int_{-\frac{\pi}{2}}^{\frac{\pi}{2}}\int_{-eV_b}^{eV_b}(g_1+g_2)\cos\theta d\theta dE_z, \tag{21}$$

where $g_1(eV_b) = 1 - S_{NR} - R_{NR} + S_{AR} + R_{AR}$ and $g_2(eV_b) = 1 - \tilde{S}_{NR} - \tilde{R}_{NR} + \tilde{S}_{AR} + \tilde{R}_{AR}$. eV_b is the bias on the junction, S is the cross-sectional area, and θ is the incident angle for ELQs.

The normalized local conductance G_L/G_0 is plotted in Fig. 6 with different barrier heights V_0 and lengths of the superconducting region L. G_0 is the conductance of the NLSM-NLSM junction. It can obviously be seen in Fig. 6 that the local conductance decreases with the potential barrier increasing. For $L = 10\xi$, the long-junction limit, the amplitude of the oscillation for local conductance becomes large. The interface barriers weaken the conductance. If the bias is larger than the energy gap, the local conductance decreases gradually with oscillation because of the coherent tunneling. In the SC energy gap regime $eV_b < \Delta$, Andreev reflection and electron reflection coexist. The large bias ($eV_b > \Delta$) will induce weaker local Andreev reflection and electron reflection;

at the same time, the normal electron transmission process becomes dominant.

From Fig. 6 we can see that beyond the Friedel oscillations which are caused by opposite wave vectors of equal magnitude interfering, there are fast fluctuations superimposed on the slow oscillations. These are the well-known McMillan-Rowell oscillations [50], which result from the interference of the different parallel wave vectors for electrons and holes. When the size of the junction changes, the McMillan-Rowell oscillations are different.

IV. CONCLUSIONS

We studied the double local and double nonlocal Andreev reflections in a NLSM-SC-NLSM heterostructure. We found a phenomenon of eight scatterings coexisting; that is, the double Andreev reflections, the double normal reflections, the double electron transmissions, and the double crossed Andreev reflections exist simultaneously. The probabilities of these scattering processes for different parameters were systematically studied. By changing the incident quasiparticle energy, incident angle, and interfacial barrier height, the amplitude of the Andreev reflections can be controlled. The probabilities of the four Andreev reflections are almost zero near $\theta = 0$ and $V_0 = 0$. That is, a finite incident angle and a finite barrier height are necessary conditions for Andreev reflections to happen. These results enrich the understanding of Andreev reflections in nodal-line semimetal-superconducting heterostructures. In experiment, the double local and double nonlocal Andreev reflections can be probed by local and nonlocal scanning tunneling spectroscopy; the differential conductance exhibits a spatially resolved ridge structure, in which the signature of the different Andreev reflections appears.

ACKNOWLEDGMENTS

This work was supported by the National Natural Science Foundation of China (Grant No. 11874139) and the Natural Science Foundation of Hebei Province (Grant No. A2019205190).

[1] C. W. J. Beenakker, Phys. Rev. Lett. **97**, 067007 (2006).
[2] C. W. J. Beenakker, Rev. Mod. Phys. **80**, 1337 (2008).
[3] Q. Zhang, D. Fu, B. Wang, R. Zhang, and D. Y. Xing, Phys. Rev. Lett. **101**, 047005 (2008).
[4] A. R. Akhmerov and C. W. J. Beenakker, Phys. Rev. B **75**, 045426 (2007).
[5] Q.-F. Sun, J. Wang, and T.-H. Lin, Phys. Rev. B **59**, 3831 (1999).
[6] K. T. Law, P. A. Lee, and T. K. Ng, Phys. Rev. Lett. **103**, 237001 (2009).
[7] H.-H. Sun, K.-W. Zhang, L.-H. Hu, C. Li, G.-Y. Wang, H.-Y. Ma, Z.-A. Xu, C.-L. Gao, D.-D. Guan, Y.-Y. Li, C. Liu, D. Qian, Y. Zhou, L. Fu, S.-C. Li, F.-C. Zhang, and J.-F. Jia, Phys. Rev. Lett. **116**, 257003 (2016).
[8] K. A. Madsen, E. J. Bergholtz, and P. W. Brouwer, Phys. Rev. B **95**, 064511 (2017).
[9] K. Li and Y.-Y. Zhang, Phys. Rev. B **94**, 165441 (2016).
[10] A. F. Andreev, Zh. Eksp. Teor. Fiz. **46**, 1823 (1964) [Sov. Phys. JETP **19**, 1228 (1964)].
[11] S.-G. Cheng, Y. Xing, J. Wang, and Q.-F. Sun, Phys. Rev. Lett. **103**, 167003 (2009); S.-G. Cheng, H. Zhang, and Q.-F. Sun, Phys. Rev. B **83**, 235403 (2011).
[12] Y. Xing, J. Wang, and Q.-F. Sun, Phys. Rev. B **83**, 205418 (2011).
[13] Z. Hou and Q.-F. Sun, Phys. Rev. B **96**, 155305 (2017).
[14] Q. Cheng, Z. Hou, and Q.-F. Sun, Phys. Rev. B **101**, 094508 (2020).
[15] A. A. Burkov, M. D. Hook, and L. Balents, Phys. Rev. B **84**, 235126 (2011).
[16] C.-K. Chiu and A. P. Schnyder, Phys. Rev. B **90**, 205136 (2014).
[17] C. Fang, Y. Chen, H.-Y. Kee, and L. Fu, Phys. Rev. B **92**, 081201(R) (2015).
[18] J.-T. Wang, H. Weng, S. Nie, Z. Fang, Y. Kawazoe, and C. Chen, Phys. Rev. Lett. **116**, 195501 (2016).
[19] Z. Yan, P.-W. Huang, and Z. Wang, Phys. Rev. B **93**, 085138 (2016).
[20] M. A. N. Araújo and L. Li, Phys. Rev. B **98**, 155114 (2018).
[21] Y. Huh, E.-G. Moon, and Y. B. Kim, Phys. Rev. B **93**, 035138 (2016).
[22] Y. Gao, Y. Chen, Y. Xie, P.-Y. Chang, M. L. Cohen, and S. Zhang, Phys. Rev. B **97**, 121108(R) (2018).
[23] K. Moors, A. A. Zyuzin, A. Y. Zyuzin, R. P. Tiwari, and T. L. Schmidt, Phys. Rev. B **99**, 041116(R) (2019).
[24] D.-S. Ma, J. Zhou, B. Fu, Z.-M. Yu, C.-C. Liu, and Y. Yao, Phys. Rev. B **98**, 201104(R) (2018).
[25] A. Martín-Ruiz and A. Cortijo, Phys. Rev. B **98**, 155125 (2018).
[26] H. Yang, R. Moessner, and L.-K. Lim, Phys. Rev. B **97**, 165118 (2018).
[27] L. Oroszlány, B. Dóra, J. Cserti, and A. Cortijo, Phys. Rev. B **97**, 205107 (2018).
[28] J. Liu and L. Balents, Phys. Rev. B **95**, 075426 (2017).
[29] J. Behrends, J.-W. Rhim, S. Liu, A. G. Grushin, and J. H. Bardarson, Phys. Rev. B **96**, 245101 (2017).
[30] M. Koshino and I. F. Hizbullah, Phys. Rev. B **93**, 045201 (2016).
[31] C. Li, C. M. Wang, B. Wan, X. Wan, H.-Z. Lu, and X. C. Xie, Phys. Rev. Lett. **120**, 146602 (2018).
[32] R. A. Molina and J. González, Phys. Rev. Lett. **120**, 146601 (2018).
[33] W. Chen, H.-Z. Lu, and O. Zilberberg, Phys. Rev. Lett. **122**, 196603 (2019).
[34] W. Chen, K. Luo, L. Li, and O. Zilberberg, Phys. Rev. Lett. **121**, 166802 (2018).
[35] S. Barati and S. H. Abedinpour, Phys. Rev. B **96**, 155150 (2017).
[36] Y.-R. Hao, L. Wang, and D.-X. Yao, Phys. Rev. B **99**, 165406 (2019).
[37] Y. Hu, H. Liu, H. Jiang, and X. C. Xie, Phys. Rev. B **96**, 134201 (2017).

[38] W. Chen, D. N. Shi, and D. Y. Xing, Sci. Rep. **5**, 7607 (2015).
[39] J. Sánchez-Cañizares and F. Sols, Phys. B (Amsterdam, Neth.) **252**, 304 (1998).
[40] M. Flöser, D. Feinberg, and R. Mélin, Phys. Rev. B **88**, 094517 (2013).
[41] C. Benjamin and J. K. Pachos, Phys. Rev. B **78**, 235403 (2008).
[42] J. Cayssol, Phys. Rev. Lett. **100**, 147001 (2008).
[43] H. Mohammadpour and A. Asgari, Phys. Lett. A **375**, 1339 (2011).
[44] X.-S. Li, S.-F. Zhang, X.-R. Sun, and W.-J. Gong, New J. Phys. **20**, 103005 (2018).
[45] Q.-F. Sun and X. C. Xie, J. Phys.: Condens. Matter **21**, 344204 (2009).
[46] U. Khanna, D. K. Mukherjee, A. Kundu, and S. Rao, Phys. Rev. B **93**, 121409(R) (2016).
[47] L. S. Xie, L. M. Schoop, E. M. Seibel, Q. D. Gibson, W. Xie, and R. J. Cava, APL Mater. **3**, 083602 (2015).
[48] Y. H. Chan, C.-K. Chiu, M. Y. Chou, and A. P. Schnyder, Phys. Rev. B **93**, 205132 (2016).
[49] G. E. Blonder, M. Tinkham, and T. M. Klapwijk, Phys. Rev. B **25**, 4515 (1982).
[50] J. M. Rowell and W. L. McMillan, Phys. Rev. Lett. **16**, 453 (1966).